Reactive oxygen species responsive double-locked liposome collaborative photodynamic therapy for reducing electrical conduction recurrence after radiofrequency catheter ablation

Ying Zhuge [a,b,1], Gonghao Li [a,c,1], Mingyue Sun [d,1], Jiajia Zhang [d], Jiafeng Zou [d], Feng Gao [d,e,f,g,*], Fang Wang [a,b,**]

[a] *Department of Cardiology, Shanghai General Hospital of Nanjing Medical University, Shanghai 200800, China*
[b] *Department of Cardiology, Shanghai General Hospital, Shanghai Jiao Tong University School of Medicine, Shanghai 200800, China*
[c] *Department of Cardiology, Lianyungang Clinical College of Nanjing Medical University, Lianyungang 222000, China*
[d] *Shanghai Frontier Science Center of Optogenetic Techniques for Cell Metabolism, School of Pharmacy, East China University of Science and Technology, Shanghai 200237, China*
[e] *Shanghai Key Laboratory of Functional Materials Chemistry, East China University of Science and Technology, Shanghai 200237, China*
[f] *Shanghai Key Laboratory of New Drug Design, School of Pharmacy, East China University of Science and Technology, Shanghai 200237, China*
[g] *Optogenetics and Synthetic Biology Interdisciplinary Research Center, State Key Laboratory of Bioreactor Engineering, East China University of Science and Technology, Shanghai 200237, China*

ABSTRACT

Radiofrequency catheter ablation (RFCA) is the preferred technique for the treatment of atrial fibrillation, but the recovery of electrical conduction after ablation seriously endangers the health of patients. This study aimed to develop reactive oxygen species (ROS) responsive double-locked liposome collaborative photodynamic therapy (PDT) to target the ablation area and reduce the recovery of electrical conduction after ablation. The successful synthesis of β-cyclodextrin modified with phenylboronic acid pinacol ester (OCD) was confirmed by ^{1}H NMR and FT-IR. Furthermore, the successful synthesis of octadecylamine-modified indocyanine green (ICG-ODA) was confirmed by ^{1}H NMR and mass spectrometry. The ICG-ODA was encapsulated in liposomes to generate a double-locked hybrid liposome (ICG-ODA@rNP), which was subsequently characterized. Several properties of ICG-ODA@rNP were evaluated, including the drug release, targeting ability and ability to inhibit electrical conduction recurrence. Moreover, a model was constructed for the blockage of electrical conduction after RFCA in rabbits to further evaluate ICG-ODA@rNP. The preliminary safety evaluation of ICG-ODA@rNP was also performed. The ICG-ODA@rNP with a uniform particle size showed excellent storage stability. The nanoparticle can sensitively release drugs under ROS environment, and exhibits excellent photothermal effects. Furthermore, ICG-ODA@rNP can circulate for a long time *in vivo* and accumulate significantly in the ablation area. In a pacing test with a left atrial appendage (LAA), these nanoparticles, combined with PDT, reduced the ratio of electrical conduction recovery, which was confirmed by a hematoxylin and eosin (H&E) test. Further molecular analysis revealed that ICG-ODA@rNP could increase RFCA-induced apoptosis and ROS levels. Specifically, ICG-ODA@rNP significantly increased the expression of Bax and cleaved caspase-3, and decreased the expression of Bcl-2. In addition, the excellent biosafety of the double-locked nanoparticle was verified. This study provides evidence that ICG-ODA@rNP, with the double lock characteristic and biosafety, which exhibits a targeting effect on RFCA-induced cardiac injury areas, which further reduce electrical conduction recovery in RFCA areas by collaborativing PDT.

* Corresponding author at: Shanghai Frontier Science Research Base of Optogenetic Techniques for Cell Metabolism, School of Pharmacy, East China University of Science and Technology, 130 Meilong Road, Shanghai 200237. China.
** Corresponding author at: Department of Cardiology, Shanghai General Hospital of Nanjing Medical University, Shanghai 200800, China.
E-mail addresses: fgao@ecust.edu.cn (F. Gao), onlyfang1@163.com (F. Wang).
[1] These authors contributed equally.

1. Introduction

Radiofrequency catheter ablation (RFCA) is a commonly employed medical intervention for the treatment of cardiac arrhythmias. Fundamentally, RFCA obstruct the pathway by which anomalous electrical activities are conducted, ceasing arrhythmia (Darby, 2016). However, studies have shown that the success rate of RFCA in the treatment of persistent atrial fibrillation is only 41.8% (Adragao et al., 2016), and the postoperative atrial fibrillation (AF) recurrence is caused by the recovery of electrical conduction in the ablation area (Odutayo et al., 2016). As postoperative recurrence of arrhythmias forces occurs at high rates, patients must undergo additionally surgeries, which increases surgical risks and economic costs.

Nanotechnology is a viable solution to ameliorate therapeutic outcomes and diminish the frequency of recurrence (Liu et al., 2022). According to our previous research, liposome loaded with drugs can effectively kill acutely injured cardiomyocytes by increasing reactive oxygen species (ROS) levels, and upregulating the expression of Bax and cleaved caspase-3 and downregulating the expression of Bcl-2 (Ying et al., 2019). Furthermore, the liposomal therapy exhibits the cardio-targeting properties due to ability of the nanodrug delivery system to target inflammation (Etrych et al., 2019; Issac et al., 2007; Katsuki et al., 2017; Li et al., 2018b; Lim et al., 2014; Moghimi et al., 2005). However, liposomes cannot be controlled due to insufficient targeting and toxic side effects in non-ablative areas (Ying et al., 2016). Fortunately, the high-ROS environment at the ablation site and the use of ROS-responsive materials provides a new way to achieve disease-specific treatment and reduce off-target toxicity. In the aftermath of RFCA, the cardiac necrotic zones manifest a pronounced inflammatory response accompanied by an acute increase in ROS (Issac et al., 2007; Lellouche et al., 2009; Lim et al., 2014). Additionally, nanoparticles constructed from ROS-responsive materials can avoid phagocytosis by the reticulo-endothelial system, which improve the delivery efficiency and therapeutic efficacy (Cormode et al., 2008). Furthermore, β-cyclodextrin modified with phenylboronic acid pinacol ester (OCD) has attracted widespread attention (Li et al., 2020; Zhang et al., 2017; Zhang et al., 2019). In the presence of hydrogen peroxide (H_2O_2), OCD hydrolyzes into water soluble products, leading to elimination of H_2O_2, disruption of the nanocontainer, and release drug. However, the drug loading and modifiability of OCD remain challenges.

Our previous studies have shown that mixing lipid materials with functional materials can improve the modifiability and stability of the materials while increasing drug loading (Sun et al., 2021; Zou et al., 2023). Therefore, combining OCD and liposomes to construct hybrid liposomes (rNP), as a drug release lock, can lead to improvements regarding the uncontrolled release of liposomes and broaden the application prospects of lipid and ROS response materials in the field of heart disease. Nevertheless, the systemic dissemination of inflammatory mediators and cytokines *via* the circulatory network, along with ROS generation, is precipitated by tissue damage and alterations in surgical interventions (Lim et al., 2013; Magnani et al., 2020; Sprague and Khalil, 2009). Additionally, drug release behavior is difficult to accurately control due to fluctuations in ROS levels at focal sites, limiting the application of rNP in the cardiac field (Lim et al., 2013; Magnani et al., 2020; Sprague and Khalil, 2009). Moreover, myocardial cells have no special target proteins other than the inflammatory environment caused by ablative damage in the ablated area. This makes it difficult to achieve the accurate release of ablation region in spatiotemporal level. Consequently, it still needs another drug release lock to further increase ROS level in the ablation region and promoting the release of nanoparticles at spatiotemporal level.

The photodynamic therapy (PDT), a noninvasive treatment modality, introduces a novel dimension to therapy (Brown et al., 2004). PDT activates hydrophobically modified indocyanine green (ICG-ODA) at spatiotemporal level to produce ROS in the presence of oxygen, triggering cell death (Correia et al., 2021). As another drug release lock, PDT furnishes an advanced degree of spatiotemporal modulation for drug release mechanisms owing to the inherent precision of laser exposure, thereby substantially mitigating systemic adverse effects. Moreover, based on the great compatibility between ICG-ODA and lipid materials (Li et al., 2018a), we believe that rNP can be effectively loaded with ICG-ODA to achieve double-locked response in combination with PDT and reduce electrical conduction recurrence.

In brief, this study aimed to develop an innovative double-locked hybrid liposome by combining ROS responsiveness and PDT (Fig. 1). Primarily, the ROS responsive carrier materials OCD was synthesized and boronic pinacol verified (Li et al., 2020). Then, the ICG-ODA synthesized in this study, was encapsulated in liposomes, which were further coupled with PEG. The above obtained double-locked hybrid liposome (ICG-ODA@rNP), which has a uniform particle size and great stability, can preferentially release drugs in a high ROS microenvironment (Li et al., 2018a). Furthermore, OCD disintegration was accelerated by the self-supplying ROS after PDT. This disintegration further promoted the rapid release of ICG-ODA and increased ICG-ODA accumulation in heart injury regions to achieve double lock responsive release and cardiomyocyte apoptosis at the ablation site. Finally, we further explored the targeting, safety, efficacy and therapeutic mechanism of ICG-ODA@rNP *in vivo* through cardiac ablation in rabbits. Through this unique dual response strategy, the above system is expected to accurately target the lesion area, providing a new method for reducing electrical conduction recurrence after RFCA.

2. Materials and methods

2.1. Materials and animals

The following reagents were acquired from Sigma Aldrich (Burlington, MA, USA): 1, 2-distearoyl-sn-glycero-3-phosphoethanolamine-N-[methoxy (polyethylene-glycol)-2000] (DSPE-PEG2000), IR775, indocyanine green (ICG), dihydroethidium (DHE) and *N*, *N*-dimethylformamide (DMF). Phenylboronic acid pinacol ester (PBAP) and 1,1-carbonyldiimidazole (CDI) were provided by Acro Organics. Octadecylamine (ODA) and β-cyclodextrin (β-CD) were purchased from Shanghai Titan Technology Co., Ltd. (Shanghai, China). Cholesterol (Chol) was purchased from Sinopharm Chemical Reagent Co. Ltd. (Shanghai, People's Republic of China). Phosphatidylcholine (PC) was purchased from Lipoid GmbH Co. Ltd. (Ludwigshafen am Rhein, Germany). 1-ethyl-3-(3-dimethylaminopropyl) carbodiimide (EDC) was purchased from Damas (Shanghai, China). Phosphate-buffered saline (PBS) was purchased from Gibco (Grand Island, NY, USA). 4% Poly-formaldehyde fixing solution, 2, 2′-azino-bis (3-ethylbenzthiazoline-6-sulfonic acid) (ABTS), fluorescein isothiocyanate (FITC) staining kit, and apoptosis detection kit were obtained from Shanghai Moukang Pharmaceutical Technology Co., Ltd. (Shanghai, China). The enzyme-linked immunosorbent assay (ELISA) kit of creatine kinase (CK), creatine kinase isoenzyme (CK-MB), lactate dehydrogenase (LDH), and cardiac troponin I (cTn—I) was purchased from Shanghai Enzyme-linked Biotechnology Co., Ltd. (Shanghai, China). The ELISA kit of Alanine aminotransferase (ALT), aspartate aminotransferase (AST), blood urea nitrogen (BUN), and creatinine (Cr) was purchased from Nanjing Jiancheng Bioengineering Institute (Jiangsu, China). Pentobarbital and Sodium Chloride Injection were purchased from MP Biomedicals (California, USA). All other reagents used in this study were analytically pure grade.

New Zealand white rabbits (8–12 months, 2–4 kg, male) used in the experiments were purchased from Jiesijie Experimental Animal Co., Ltd. (Shanghai, China) and acclimatized to a specific pathogen-free environment under controlled conditions (22 ± 2 °C, 12 h light/dark cycle) for one week. The animal experiments were carried out in accordance with the guidelines evaluated and approved by the ethics committee of East China University of Science and Technology (IACUC-IRB number: 2023AWS052).

2.2. Synthesis of OCD and ICG-ODA

PBAP (1.11 g, 4.72 mmol) was completely dissolved in anhydrous dichloromethane (DCM) by ultrasound. CDI (1.53 g, 9.29 mmol) was then added into the above solution with vigorous stirring for 2 h at 25 °C to fully activate the PBAP. After adding DCM, the mixture was washed with deionized water (3 × 10 mL). The organic phase was collected and further washed with saturated $NaCl_2$ solution (3 × 20 mL). Then anhydrous sodium sulfate solid was added to the organic phase, and the organic solvent was volatilized with a vacuum pump to obtain a dry activated solid (CDI-PBAB). CDI-PBAP was characterized by ^{1}H NMR spectroscopy (Zhang et al., 2017).

The CDI-PBAP obtained above was dissolved in anhydrous DMSO, into which β-CD (0.125 g, 0.11 mmol) and DMAP were added. The obtained mixture was magnetically stirred at 25 °C for 24 h. The product was washed with deionized water and collected by centrifugation. The sample was subjected to lyophilization, resulting in a white powder that constitutes the ROS-responsive OCD (Zhang et al., 2017). The final product was characterized by ^{1}H NMR and Fourier transform infrared (FT-IR) spectroscopy.

Based on a molar ratio ICG to EDC to DMAP at 1:3:3, ICG (6.75 mg/mL, dissolved in DMF) were mixed with EDC, DMAP (1 mg/mL, dissolved in deionized water). The mixture was stirred for 1 h at 45 °C in the dark, and then octadecylamine (ODA, 7.5 mg/mL, dissolved in DMF) was added and stirred for another 24 h (Li et al., 2018a). The reaction solution was dialyzed with a dialysis bag (MWCO: 3.5 k Da) for 48 h and collected after lyophilization. The final product (ICG-ODA) was characterized by ^{1}H NMR and mass spectroscopy (Xevo® G2 Tof, Waters, USA).

2.3. Preparation of nanoparticles

PC, Chol, and DSPE-PEG2000 were dispersed in 0.5 mL of ethanol, which added with 4 mL deionized water and then heated in a water bath at 65 °C for 1 h (Zhang et al., 2019). OCD and ICG-ODA were dispersed in 2 mL of methanol, and then slowly added dropwise to the aforementioned solution. After incubating for 2 h, the drug-loaded nanoparticles, termed ICG-ODA@rNP, were obtained.

2.4. Characterization of the nanoparticles

The mean particle size, polydispersity index (PDI), and zeta potential of ICG-ODA@rNP were measured by dynamic light scattering (DLS) using a Nano-ZS90 Zetasizer (Malvern, UK). The morphology of ICG-ODA@rNP was examined by transmission electron microscopy (TEM). Briefly, 10 μL of ICG-ODA@rNP sample was dropped onto the copper grids covering the carbon layer. After a period of time, the excess solution was removed, and the negative staining was performed with 2% (*w/v*) phosphotungstic acid (Zou et al., 2023), followed by observation using a JEM-2100 instrument (JEOL Ltd., Japan). The UV absorption spectra of ICG-ODA, rNP and ICG-ODA@rNP in the range of 400 to 900 nm were measured by an UV spectrometer (UV–vis, UV-1800, Schimadzu, USA). The loading efficiency (LE) and encapsulation efficiency (EE) of ICG-ODA@rNP were calculated.

2.5. Stability of the nanoparticles

The prepared ICG-ODA@rNP was stored at 4 °C, and the particle size, PDI and zeta potential of a certain amount of ICG-ODA@rNP were detected by DLS at the same time points on days 1, 2, 3, 5, 7, 9, 14, 21 and 28, respectively (Zou et al., 2023). The ICG-ODA@rNP stored at room temperature were characterized using the same method on 1, 7, 14, and 28 days, respectively. The storage stability of ICG-ODA@rNP was investigated by plotting the curve (Ying et al., 2019).

2.6. In vitro drug release

Different concentrations of H_2O_2 solution were designed to simulate the ROS environment in the rabbit heart during the treatment. The equal volume of ICG-ODA@rNP was incorporated into the dialysis bag (MWCO: 8-10 k Da) and then dialyzed in PBS solution at 37 °C. After 2 h, the dialysis bag was transferred to the release medium with H_2O_2 (H_2O_2 concentrations: 0, 0.1, 1.0 or 3.0 mM), respectively. In the experiment, two groups were set with a concentration of 1.0 mM H_2O_2. 1.0 mM H_2O_2 + NIR group was exposed to NIR light at a wavelength of 808 nm for 30 s, while the other group was not exposed to light. At the desired time intervals, 500 μL of release medium was withdrawn and 500 μL of fresh release medium was added. The concentration of ICG-ODA in the release medium at different time points (0, 1, 2, 3, 4, 6, 8, 12 and 24 h) was determined by an UV spectrometer (UV–vis, UV-1800, Schimadzu, USA), and the cumulative release amount was calculated (Sun et al., 2020).

2.7. Photothermal and photodynamic performances

Different groups of solutions with H_2O_2 (concentration: 20 μM) and ICG-ODA@rNP (concentration: 0, 0.1, 0.5 or 1.0 mg/mL) were prepared. Each group of mixture was added with an appropriate amount of 2, 2′-azino-bis (3-ethylbenzthiazoline-6-sulfonic acid) (ABTS) solution (Re et al., 1999). The solution to be measured was irradiated with an 808 nm NIR laser (1 W/cm^{2}) for 30 s by the fiber coupled laser module (MW-GX-808/5000 mW, Changchun Leishi Photo-Electric Technology Co., Ltd., China), and the absorbance within 300–600 nm was scanned by an UV spectrometer (UV–vis, UV-1800, Schimadzu, USA). The changes of absorbance of each group at 415 nm were compared to characterize the production of singlet oxygen, and then the photodynamic effect of ICG-ODA@rNP was investigated.

ICG-ODA@rNP solutions (concentration: 0, 0.1, 0.5 or 1 mg/mL) were prepared, and 200 μL of each solution was taken in a centrifuge tube. Each group was irradiated with an 808 nm NIR laser (1 W/cm^{2}) for 5 min. The temperature of the solution at different time points was recorded by an infrared temperature imager every 30 s. The curve of ICG-ODA@rNP solution with different concentrations changing with illumination time was drawn, and the photothermal effect at different concentrations was investigated.

2.8. RFCA operation procedures

The operation was performed using aseptic techniques and sterile instruments. Rabbits were fitted with a breathing mask before surgery, which was connected to a ventilator. Then, rabbits were anesthetized by inhalation of 3% Isoflurane. After the corneal reflex disappeared, rabbits were placed supine on a 37 °C thermostatic operating platform. Open the chest cavity in the fourth intercostal space, then use a chest dilator to expose the entire heart. A small incision is made in the pericardium to expose the myocardial wall, and the LAA is gently removed with a hemostatic forceps.

Before ablation, the ablation catheter (Celsius,Biosense Webster Inc., Irwindale, CA, USA) and the negative plate were connected to the cardiac ablation generator (IBI-1500 T8, Irvine Biomedical Inc., Irvine, CA, USA), which was set to power control mode (power = 10 W). Circumferential ablation was then performed on the anterior and posterior walls of the LAA using ablation catheters. The criteria for each ablation endpoint were as follows: (1). The ablation points are connected with each other to form a complete closed-loop form; (2). Pacing tests were performed at the distal end of the LAA, which confirmed electrical block in the ablation area (Ying et al., 2019).

After ablation and electrophysiological examination, the wound of the rabbits was sutured immediately and wrapped with sterile gauze. Then, the rabbits were injected with drugs through the ear vein. After the operation, the health status of the rabbits was monitored, including

the observation of their activity level, dietary intake and wound healing.

2.9. Electrophysiological recordings and pacing tests

Electrocardiogram, epicardial potential and pacing signals were recorded using a cardiac electrophysiological recording system. Epicardial potential was collected by the bipolar electrode catheter touching the LAA or the left atrium.

The pacing test was used to evaluate the electrical conduction of the ablation area. The pacing electrode catheter was placed at the distal end of the LAA to perform the S1S1 pacing procedure. The pacing rate was set faster than the rabbit sinus rhythm (RR-S1S1 $\geq$ 30 ms). At the same time, another mapping electrode catheter touched the left atrium and recorded the left atrial potential (A-wave) (Ying et al., 2019).

Electrical conduction in the ablation area was evaluated by comparing the pacemaker signal (S1) with the left atrial potential (A-wave). When S1S1 procedure was implemented, electrical conduction was considered normal if S1 and A waves exhibit A 1:1 correspondence (AA = S1S1). Conversely, if the A wave is unrelated to the S1 wave, electrical block was considered to have occurred in the ablation area, in which case the AA phase did not change before and after the pacing test.

The same pacing tests were performed before ablation, immediately after ablation, and 10 days after ablation.

2.10. Experiment of pharmacokinetic

New Zealand white rabbits were fasted and drank normal water the night before the experiment. The rabbits were randomly divided into 3 groups, 4 in each group. The LAA of rabbits in group RFCA, RFCA + ICG-ODA + NIR, and RFCA + ICG-ODA@rNP + NIR were ablated after thoracotomy. After 24 h, group RFCA + ICG-ODA + NIR was injected with 2 mg/kg ICG-ODA solution through the ear vein, and group RFCA + ICG-ODA@rNP + NIR was injected with 2 mg/kg ICG-ODA@rNP solution through the ear vein. Both groups of rabbits were injected with a certain amount of antibiotics to prevent infection and were fed normally.

After administration, an appropriate amount of blood was taken from the rabbit ear vein at set time points (5 min, 0.5, 1, 2, 4, 6, 8, 12 and 24 h), and normal saline was supplemented. The rabbit blood samples of group of RFCA + ICG-ODA + NIR, and RFCA + ICG-ODA@rNP + NIR were centrifuged at 8000 rpm/min for 10 min to separate the upper plasma. Plasma samples were centrifuged again after precipitating proteins and volumetric fixation, and stored at $-20\ ^\circ$C. The content of ICG-ODA in rabbit blood was detected by lumina fluorometer (Thermo Fisher Scientific, USA). Two groups of rabbits were sacrificed at 24 h and 48 h. The heart and other main organs were collected for detecting the ICG-ODA content in organs.

2.11. Biodistribution and cardiac-targeting ability of the ICG-ODA@rNP

To conduct the study of fluorescence imaging biodistribution, we prepared IR775-labeled hybrid liposome (IR775@rNP). Rabbits in the control group were fed normally without any operation. Rabbits in the experimental group were injected with free IR775 and IR775@rNP (0.5 mg/kg) into the ear vein at 24 h after RFCA (Ying et al., 2019). Some rabbits were sacrificed at 48 h and 72 h. The hearts and other main organs of each group were removed and washed with normal saline (Yan et al., 2013). The *in vivo* imaging system (FX-PRO, Carestream Health, USA) (excitation wavelength 740 nm and emission wavelength 790 nm) was used to image each group of organs.

2.12. In vivo therapeutic efficacy

Ten adult New Zealand White rabbits were modeled as described above and were further used to evaluate the effect of ICG-ODA@rNP on electrical conduction recurrence. Rabbits were randomly divided into two groups, including the ablation combined saline group and the ablation combined ICG-ODA@rNP group. Saline and ICG-ODA@rNP were injected intravenously *via* the ear vein (2 mg/kg) at 24 h after ablation (Ying et al., 2019). All rabbits underwent thoracotomy after 24 h of administration, and then the ablation area was irradiated with a laser at 808 nm wavelength for 5 min (1 W/cm^2). Pacing test was performed immediately and within 10 days after ablation, and electrocardiogram (ECG) was recorded simultaneously.

Rabbits were randomly divided into four groups, including the control group, RFCA group, RFCA combined ICG-ODA group, and RFCA combined ICG-ODA@rNP group. ICG-ODA and ICG-ODA@rNP were administered at 1 mg/kg, and other experimental operations were consistent with the above. Rabbits were sacrificed on 1 and 10 days, and the ablation sites of LAA were isolated and washed with saline. The samples were fixed with paraformaldehyde (4%), embedded in paraffin wax, stained with hematoxylin and eosin (H&E) (Zou et al., 2023), followed by analyzed *via* digital tissue section scanner (Pannoramic MIDI, 3DHISTECH Ltd., Hungary).

In order to verify that ICG-ODA@rNP can enhance ROS in the ablation site, fresh LAA sections were stained with DHE (Chen et al., 2024). Then, the marked LAA sections were then exposed to DAPI after washing with PBS. The fluorescence microscope (TI-SR, Nikon, Japan) was used to shoot the stained sections, and the fluorescence intensity was analyzed by ImageJ software.

Apoptotic cells were detected by terminal deoxynucleotidyl transferase-mediated deoxyuridine triphosphate nick end labeling (TUNEL) assay using the cell death detection kit (Zou et al., 2023).

The left atrial appendage of the rabbit was fixed with 4% paraformaldehyde, followed by paraffin embedding and preparation of sections. Next, the dewaxing and rehydration steps of the slices were performed, and then the antigen was repaired with 10 mmol/L sodium citrate (pH 6). The slices were immersed in 3% H_2O_2 for 30 min to remove the activity of endogenous catalase. Subsequently, the samples were blocked with PBS containing 1% (*w/v*) bovine serum albumin for 60 min. Then, different primary antibodies (Bax antibody, Bcl-2 antibody, Cleaved caspase-3 antibody) were added to each group of samples, and the slices were incubated overnight at 4 $^\circ$C. Subsequently, horseradish peroxidase (HRP)-labeled secondary antibody was added to the sample and waited for 2 min after coating with 3,3'-Diaminobenzidine (DAB) reagent. Then the DAB was washed and counter-stained with Mayer hematoxylin. Finally, the slices were scanned and imaged under a microscope using a slice scanner, and the protein expression was analyzed using ImageJ software.

2.13. Toxicity evaluation

After therapy, blood was taken from the ear vein of rabbits, which was then centrifuged to get the albumin for the aspartate aminotransferase (AST), alanine aminotransferase (ALT), creatinine (Cr), and blood urea nitrogen (BUN) kit-test. Four groups of rabbits were taken 1 mL blood at the set time point, and the samples were centrifuged at 8000 rpm/min for 10 min to obtain the supernatant. Creatine kinase (CK), creatine kinase isoenzyme (CK-MB), lactate dehydrogenase (LDH), and cardiac troponin I (cTn-I) in blood samples were quantified using appropriate ELISA kits according to the manufacturer's instructions (Ramasamy, 2011; Zou et al., 2023). The major organs (heart, liver, spleen, lung and kidney) of the rabbits were collected. Histopathological sections were prepared and stained with H&E.

2.14. Statistical analysis

Data analyses were carried out using Prism 9.0 (GraphPad, La Jolla, CA, USA) *via* one-way analysis of variance (ANOVA) with Tukey's *post hoc* test. A value of $P < 0.05$ was considered statistically significant.

3. Results and discussion

3.1. Synthesis of OCD and ICG-ODA

To generate OCD, chemical functionalization of β-CD was performed with the oxidation-labile compound PBAP (Fig. S1). β-CD was used as a scaffold molecule due to its multiple advantages, such as low cost, good *in vivo* safety, and ability to be incorporated with various compounds. Characterization by FT-IR and ^{1}H NMR spectroscopy indicated that OCD was successfully synthesized (Fig. S2 A-B). The FT-IR spectra of OCD showed characteristic peaks of the benzene ring at 1650–1563 cm^{-1} and C=O at 1745 cm^{-1}. Compared with that of β-CD, the intensity of the peak attributed to the hydroxyl groups at 3330 cm^{-1} of OCD decreased significantly. Calculations based on the ^{1}H NMR spectrum revealed that the 7 CDI-PBAP units were conjugated to each β-CD molecule (Feng et al., 2016).

A hydrophobic modification was performed by conjugating the amino groups on ODA with the sulfonic groups on ICG to effectively encapsulate ICG (Fig. S3). The ^{1}H NMR spectra revealed that the amino group peak of ICG-ODA at 2.7 ppm was significantly weaker than that of ODA (Fig. S4). The mass spectrum demonstrated that there could be one or two ODA molecules conjugated on one ICG molecule, indicating the molecular weight of ICG-ODA was 1044.5 and 1291.9 (Fig. S5). This result indicated that the amino groups on the ODA connected successfully with the sulfonic groups on ICG, and a dehydration reaction occurred between the two groups to generate ICG-ODA (Fig. 1). The yield of ICG-ODA was 75.5%.

3.2. Characterization of the nanoparticles

Table. S1 summarizes the physicochemical properties of the ICG-ODA-loaded nanoparticles. The mean hydrodynamic diameter of the ICG-ODA@rNP was 126.6 ± 2.6 nm (Fig. 2A), the zeta potential was −8.6 ± 0.4 mV, and the PDI was 0.19. The LE of ICG-ODA@rNP was 9.4 ± 0.2%, and the EE was 71.8 ± 1.8%. Characterization by TEM suggested that ICG-ODA@rNP exhibited a well-defined spherical shape and complete bilayer (Fig. 2A), with a relatively narrow size distribution. The UV absorption spectra of ICG-ODA, rNP and ICG-ODA@rNP in the range of 400 to 900 nm were measured by ultraviolet spectrophotometer. ICG-ODA@rNP showed an obvious absorption peak at 785 nm, which proved the successful synthesis of the nanoparticles and loaded ICG-ODA into the nanoparticles (Fig. S6).

3.3. Storage stability

Within 28 days of storage at 4 °C, the mean hydrodynamic diameter, zeta potential, and PDI of ICG-ODA@rNP were stable, with an average of 126.9 ± 2.8 nm, −8.9 ± 0.8 mV and 0.20, respectively (Fig. 2B and Fig. S7). No flocculation or precipitation was observed, indicating that the nanoparticles had good storage stability (Yuan et al., 2022). Additionally, we also investigated the stability of nanoparticles at room temperature in Fig. S8. The destruction of the stability of the nanoparticles at room temperature may be related to bacterial growth and other reasons.

3.4. Photothermal and photodynamic performances

In addition, we verified the photothermal performance of ICG-ODA. As the concentration of ICG-ODA@rNP increased, the warming rate of the solution system progressively accelerated (Fig. 2C). When the concentration of ICG-ODA@rNP was 1.0 mg/mL, the temperature of the solution system increased from 24.7 to 47.6 °C within 5 min after
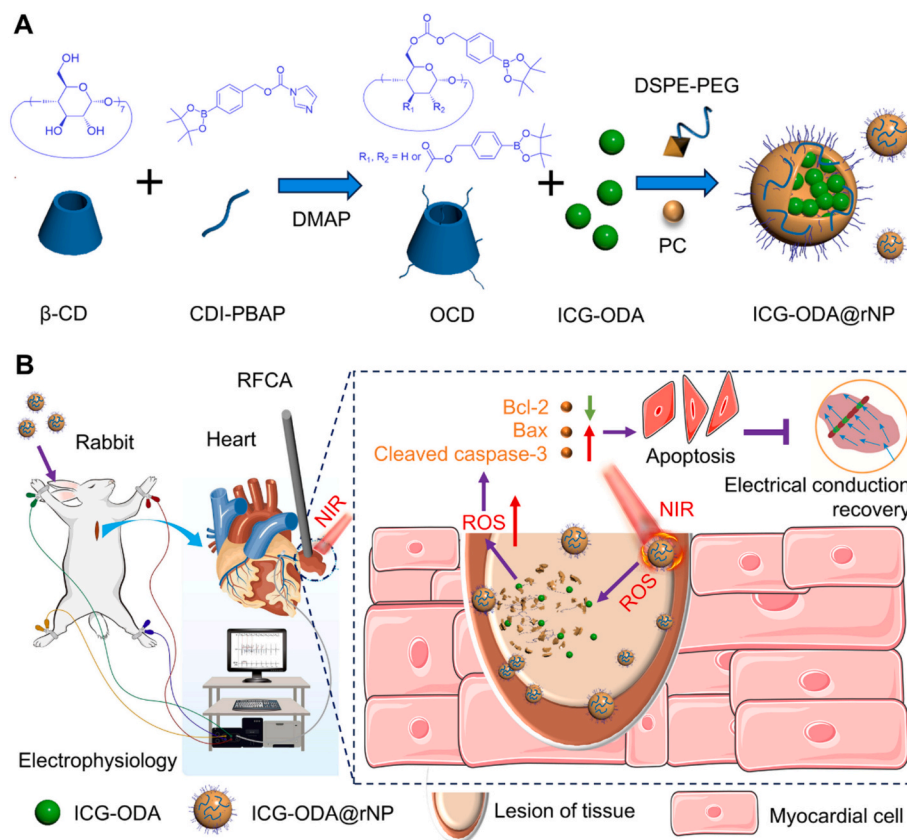

Fig. 1. Schematic diagram of the effect of ICG-ODA@rNP on cardiomyocytes. (A) The synthetic route of ICG-ODA@rNP. (B) ICG-ODA@rNP accurately targeted the ablation site of the heart through the NIR laser/ROS double-locked effect, up-regulated the expression of Bax and Cleaved calpain I, down-regulated the expression of Bcl-2, and promoted apoptosis.
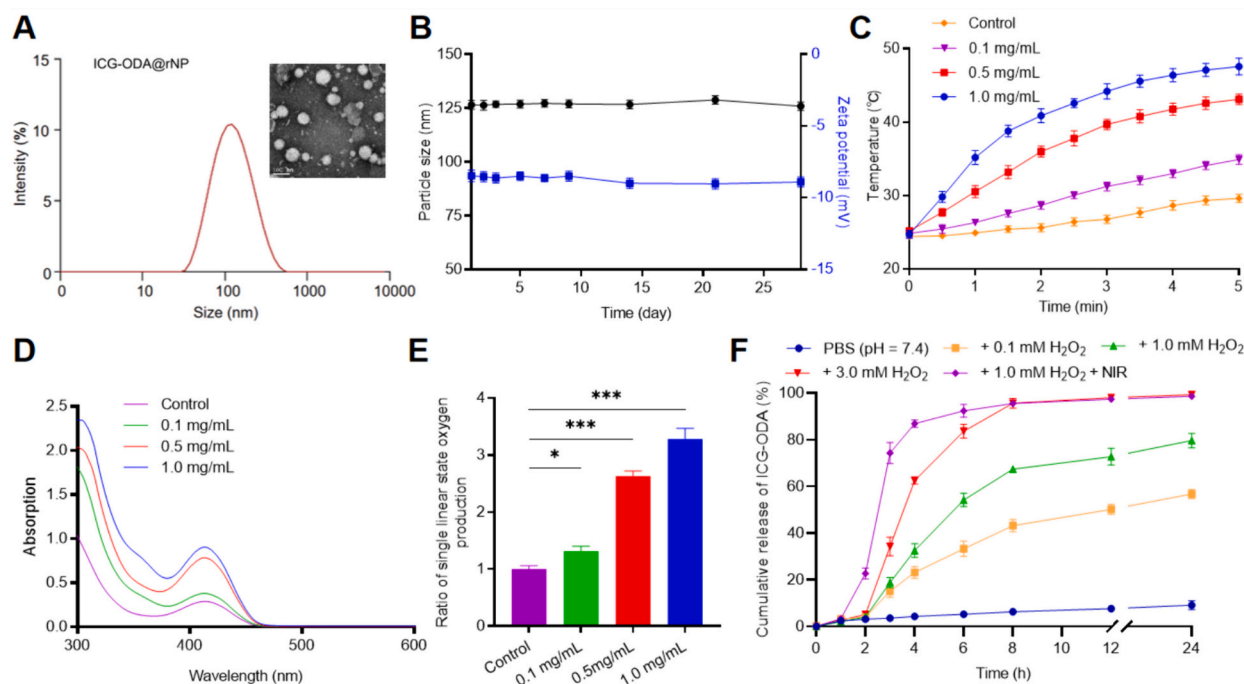
Fig. 2. Characterization of the ICG-ODA@rNP. (A) The diameter distribution and TEM images of ICG-ODA@rNP. (B) The stability of ICG-ODA@rNP over 28 d. (C) *In vitro* temperature changes of ICG-ODA@rNP after 808 nm laser irradiation. (D) The absorption spectrums of ICG-ODA@rNP after reaction with ABTS by 808 nm laser irradiation. (E) The quantitative representation of single linear state oxygen production. (F) *In vitro* drug release profiles of ICG-ODA@rNP in different groups. Compared with the control group, *$P < 0.5$, ***$P < 0.001$. Data are presented as mean $\pm$ SD ($n = 3$).

illumination, reaching an effective temperature that could kill cardiomyocytes. For the aqueous solution without nanoparticles, the system temperature only increased from 24.7 to 29.4 °C. The results showed that the photosensitivity and photothermal properties of ICG were not affected by fat-soluble modification.

ABTS is oxidized by oxidants to its radical cation, •ABTS$^+$ which is intensely colored in blue–green. The absorption peak of •ABTS$^+$ at 415 nm was pronounced (Cano et al., 2002; Munteanu and Apetrei, 2021; Re et al., 1999). ABTS can be employed as a detection reagent for singlet oxygen. The results showed that under specific dual response conditions (20 μM H_2O_2 and 808 nm NIR laser irradiation), ICG-ODA@rNP could effectively release ICG-ODA and produce singlet oxygen. The absorbance of the •ABTS$^+$ solution at 415 nm increased with increasing nanoparticle concentration, which demonstrated that the yield of singlet oxygen was dependent on the concentration of ICG-ODA@rNP (Fig. 2D-E).

3.5. In vitro drug release

In this study, the dynamic changes in ROS in the left atrial appendage ablation area (LLA) after RFCA were simulated by adjusting the concentration of H_2O_2 (0, 0.1 mM, 1.0 mM or 3.0 mM). Among them, the 0.1 and 1.0 mM H_2O_2 groups were designed to reproduce RFCA-induced local inflammation and corresponding ROS levels. With increasing of H_2O_2 concentration, the release efficiency of the nanoparticles increased significantly (Fig. 2F). The drug release mechanism may involve the oxidation of PBAP molecules connected to β-CD to phenols, followed by quinone methide rearrangement and subsequent hydroxyl group cleavage. OCD was completely hydrolyzed to produce β-CD, pinacol borate, and *p*-hydroxymethylphenol. The interaction between OCDs is weakened (Li et al., 2020; Zhang et al., 2017; Zhang et al., 2019), and the nanoparticles relaxed or dissociated, thereby releasing ICG-ODA. These results also demonstrate the potential of OCD as a drug release lock in the RFCA region.

In addition, two response conditions of 1.0 mM H_2O_2 and 808 nm

wavelength near-infrared (NIR) laser, were combined to simulate the synergistic effect of RFCA and PDT. The drug release characteristics of ICG-ODA@rNP in these environments were investigated, as shown in Fig. 2F. The experimental results showed that the drug release rate of ICG-ODA@rNP increased in the absence of NIR laser. Moreover, we simulated the RFCA area treated with a high concentration (3.0 mM) of H_2O_2 in the NIR region. Compared to the 3.0 mM H_2O_2 group, the nanoparticles showed a faster drug release rate in a 1.0 mM H_2O_2 environment with 808 nm NIR laser irradiation. This result further indicated that the released ICG-mediated self-generated ROS and temperature increase accelerated the disintegration of the nanoparticles and further promoted the rapid release of ICG-ODA after PDT. The above results also verified the double-lock release characteristics of ICG-ODA@rNP *in vitro*. However, the *in vivo* targeting and distribution characteristics of ICG-ODA@rNP remain to be further confirmed.

3.6. Ablation in the LAA region

The LAA in rabbits underwent ablation through an ablation catheter (Celsius, Biosense Webster Inc., Irwindale, CA, USA), resulting in coagulative necrosis of myocardial cells at the ablation site, accompanied by the emergence of a white ulcerated surface (Fig. 3A). Based on a prior study conducted by our team (Ying et al., 2019; Ying et al., 2016), the ablation parameters were established at a temperature of 55 °C, a power output of 15 W, and an ablation duration of 15 s. During high-frequency electrical pacing of the LAA, the RR interval was calibrated to 200 ms, and the pacing frequency was set at 300 bpm.

3.7. In vivo pharmacokinetic parameters of nanoparticle

Post-RFCA, the concentration of nanoparticles at the necrotic site holds significance for preventing the recurrence of AF (Liu et al., 2022). Fig. 3B showed the pharmacokinetic curves for the blood circulation kinetics of free ICG-ODA and ICG-ODA@rNP in the RFCA-treated rabbit model. After intravenous administration, unencapsulated ICG-ODA was
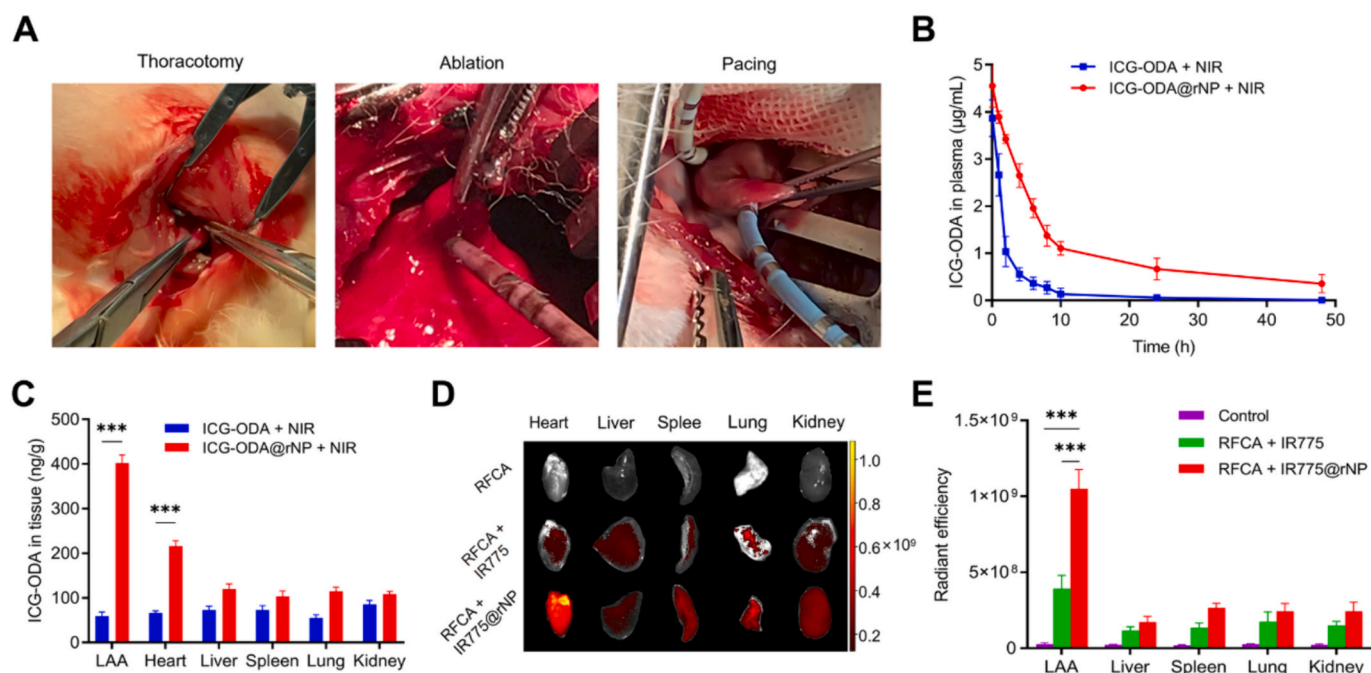
Fig. 3. (A) The thoracotomy, ablation, and pacing procedures during the RFCA process. (B) Blood concentration-time profiles in rabbits of free ICG-ODA and ICG-ODA@rNP (2 mg/kg ICG-ODA) after intravenous administration. (C) Drug distribution by tissues of ICG-ODA and ICG-ODA@rNP 48 h after ablation and drug administration in left heart ear of rabbit. (D) *In vitro* images of the organs of each group of rabbits 48 h after administration. (E) Quantification of the fluorescence intensity of each organ. Compared with the control group, ***P < 0.001. Data are presented as mean ± SD ($n = 4$).

rapidly eliminated in the liver. In contrast, ICG-ODA@rNP significantly prolonged the systemic circulation time of ICG-ODA for better absorption and retention.

The key pharmacokinetic parameters for ICG-ODA and ICG-ODA@rNP were derived and are presented in Table. S2. After an equivalent dose (2 mg/kg) was administered, the distribution half-life ($t_{1/2\alpha}$) of ICG-ODA@rNP was extended from 1.04 to 3.26 h, relative to that of ICG-ODA. Moreover, the elimination half-life ($t_{1/2\beta}$) increased from 7.73 to 29.93 h. Notably, the elimination rate constant (K_{el}) and the clearance rate (CL) for ICG-ODA were 5.71-fold and 6.23-fold greater, respectively, than those for the ICG-ODA@rNP. Additionally, the mean residence time (MRT) for ICG-ODA@rNP increased 3.01-fold. Both the AUC_{0-48h} and $AUC_{0-\infty}$ for this group significantly increased. These results suggested that liposomes can prevent ICG-ODA from binding to plasma proteins and increase the circulation time of the drug in the blood, thereby significantly reducing the drug dose necessary for subsequent treatment and reducing dose-dependent toxicity.

3.8. Biodistribution and cardiac-targeting ability of the nanoparticles

Meanwhile, compared with that in the ICG-ODA group, the ability of LAA in the ICG-ODA@rNP group to target tissue was significantly greater at 48 h post-administration. (Fig. 3C). The concentration of ICG-ODA@rNP in the LAA was approximately 6.77-fold greater than that of ICG-ODA. This increase in concentration can be attributed to cardiomyocyte necrosis and local tissue inflammation induced by RFCA, which increased the accumulation of macrophages that ingested ICG-ODA@rNP in the LAA (Kim et al., 2021; Yan et al., 2013). In addition, RFCA can increase vascular endothelial permeability (Kong et al., 2021), and thus the retention time of ICG-ODA@rNP. This finding preliminarily reveals the targeting properties of double-locked liposomes and the reduced toxic side effects.

To further clarify the targeting characteristics of ICG-ODA@rNP, drug accumulation in the heart was examined 48 and 72 h post-administration for the RFCA, RFCA + IR775, and RFCA + IR775@rNP group by employing an *in vivo* imaging system (Fig. S10A). The control

group, which was devoid of IR775, exhibited no fluorescence. In the RFCA + IR775 group, fluorescence was observed throughout the heart after 48 and 72 h, indicating that IR775 lacked specific targeting. Compared with that in the RFCA + IR775@rNP group, the distribution of IR775 was less obvious, possibly because IR775 is easily cleared in the free state within the body. At 48 h, the RFCA + IR775@rNP group showed a uniform and significant fluorescence distribution throughout the heart, especially in LAA. At 72 h, the fluorescence of other parts of the heart gradually weakened, indicating that IR775 was gradually metabolized in these areas, while the fluorescence intensity of LAA remained the most significant. This result indicates that IR775@rNP can efficiently accumulate in the ablation-treated LAA site and penetrate into the inflammatory tissue due to its long circulation periods.

The fluorescence intensity of isolated hearts in each group was quantitatively analyzed. As demonstrated in Fig. S10B, after 48 h, the fluorescence intensity of LAA in the RFCA + IR775@rNP group was 2.84-fold greater than that in the RFCA + IR775 group. At 72 h, the proportion increased 5.04-fold. As shown in Fig. S10C, the difference in fluorescence intensity were compared between LAA and right atrial appendage (RAA) in each group at 72 h, revealing that the fluorescence intensity of LAA in RFCA + IR775@OCD NP group was 4.96-fold that of RAA. These results further confirmed that IR775@rNP can optimize its distribution in target tissues, effectively accumulate in LAA, and prolong the residence time *in vivo*.

Fig. 3D shows the fluorescence distribution of each organ in the control group, RFCA + IR775 group and RFCA + IR775@rNP group at 48 h after administration. The RFCA + IR775@rNP group exhibited the strongest fluorescence intensity in each organ, especially the fluorescence of LAA was the most obvious. As shown in Fig. 3E, the quantitative analysis of fluorescence intensity further demonstrated that IR775@rNP had a notable accumulation effect on LAA after ablation. In contrast, the fluorescence intensity of each organ in the RFCA + IR775 group was substantially lower than that in the RFCA + IR775@rNP group due to the rapid metabolism of free IR775 in the body. The above results further indicated the advantageous targeting properties of double-locked liposomes, which could be used for further *in vivo* efficacy and

safety evaluation.

3.9. Ablation area tissue sections

After RFCA and subsequent pharmacological intervention, histological examination of the LAA site in rabbits was performed *via* H&E
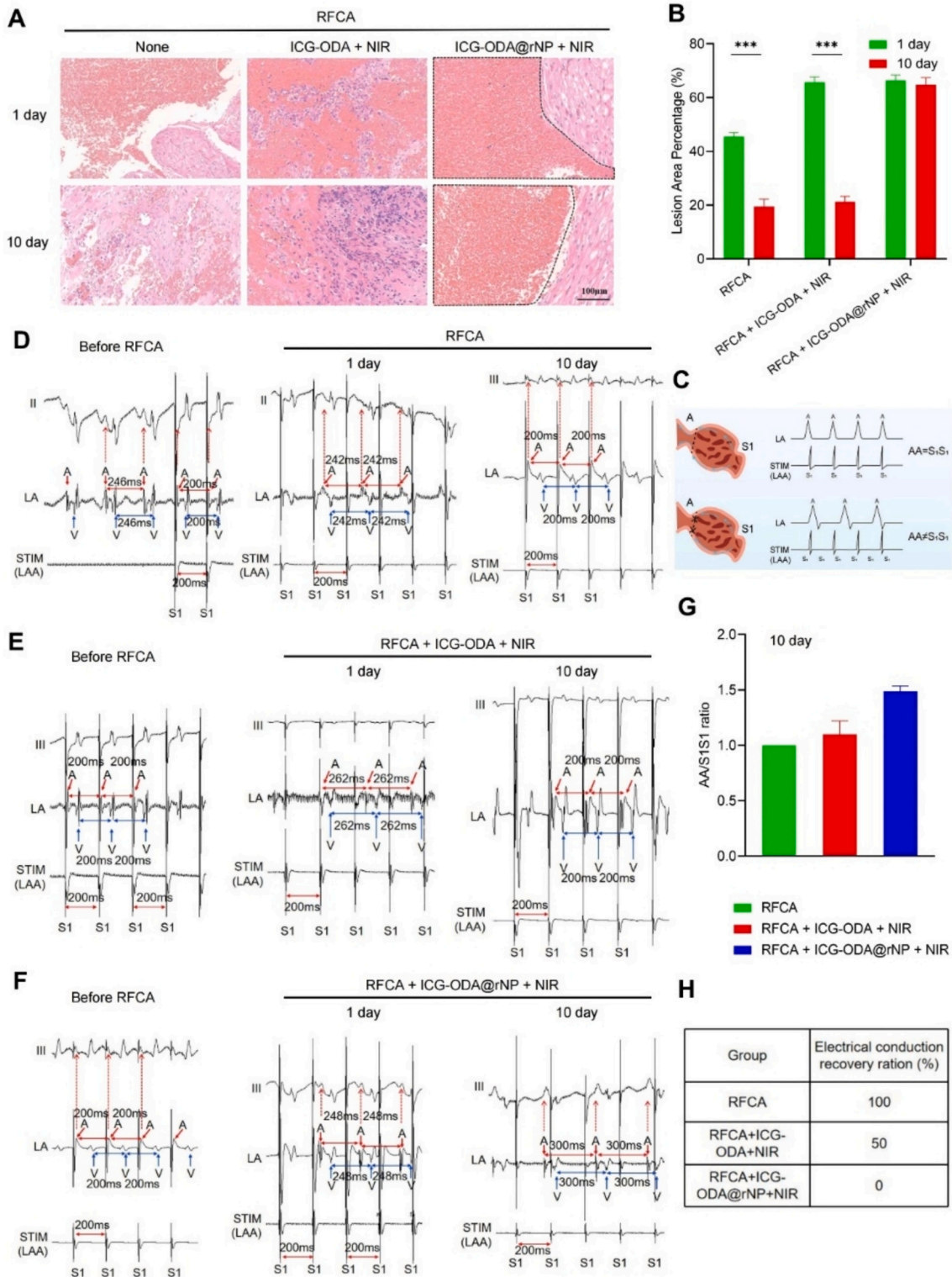

Fig. 4. (A) H&E staining of left heart ear tissue sections from different groups of rabbits after ablation on 1 and 10 day, and quantitative representation of the area of lesion as a percentage of total area (B). (C) The schematic diagram corresponding to S1 and A-waved. (D) ECG at different time points in RFCA group. (E) ECG at different time points in RFCA + ICG-ODA + NIR group. (F) ECG at different time points in RFCA + ICG-ODA@rNP + NIR group. (G) The ratio of AA/S1S1 for different groups. (H) The conduction recovery rates for different groups on 10 days. Compared with the RFCA group, ***P < 0.001. Data are presented as mean ± SD. Data are presented as mean ± SD (n = 4).

staining. The micrographs obtained after sectioning are presented in Fig. 4A-B. On the first post-operation day, the myocardial cells in the RFCA group were disrupted and the nuclear damage was obvious, showing transmural lesions, including hemorrhage, coagulation necrosis and fibrosis. These changes indicate the electrical conduction blockade occurred due to myocardial cell injury. Intriguingly, the manifestations at the myocardial ablation site appeared notably diminished, potentially attributable to intrinsic reparative mechanisms or perhaps suboptimal ablation yielding incomplete lesions at 10 days. Partial myocardial lesions tend to restore electrical functionality over time.

Within the ICG-ODA + NIR group, tissue insult was discernible on day one post-irradiation, implying that free ICG-ODA is cytotoxic to cardiomyocytes. Compared with those in the RFCA group, the lesions in this group were more profound. However, compared with those on 1 day, the tissue lesions in this group had significantly subsided by 10 days, indicating that the metabolic clearance of free ICG-ODA was rapid. Therefore, the free drug is nonspecific, has limited ability to target myocardial cells, and cannot clearly target damaged tissues, which is consistent with the above results.

The ICG-ODA@rNP group manifested more severe tissue degradation on 1 day. By 10 days, the infarcted region remained markedly compromised, effectively impeding myocardial electrical conduction. The ICG-ODA@rNP group exhibited more pronounced tissue injury on 1 day. By Day 10, the necrotic region remained notably impaired, potentially leading to effective obstruction of myocardial electrical conduction (Fig. 4B). The results confirmed that ICG-ODA@rNP had superior targeting and retention ability and that the rapid release of ICG-ODA mediated by the double-lock effect could effectively kill cardiomyocytes in the ablation area.

3.10. Electrocardiogram monitoring

ECG monitoring results have been used as a powerful means of evaluating the ability to inhibit electrical conduction recovery after RFCA (Ying et al., 2019; Ying et al., 2016). Fig. 4 C showed that S1S1 = AA (Ratio of AA/S1S1 = 1), indicating that the recovery of myocardial electrical conduction in rabbits after RFCA. In the RFCA, ICG-ODA + NIR + RFCA, and ICG-ODA@rNP + NIR + RFCA group at 1 day, S1S1 ≠ AA (Ratio of AA/S1S1 ≠ 1), indicating the recovery of myocardial electrical conduction in rabbits after RFCA. In the RFCA, ICG-ODA + NIR + RFCA, and ICG-ODA@rNP + NIR + RFCA groups at 1 day, S1S1 ≠ AA (Ratio of AA/S1S1 ≠ 1), indicating that RFCA was effective and that the electrical conduction of the LAA was successfully blocked (Fig. 4D-F). However, in the RFCA group at 10 days, S1S1 = 200 ms = AA, and the heart rate was equal to the pacing frequency, which demonstrated that cardiac pacing was achieved and that the electrical conduction of the myocardium was restored. In contrast, in the ICG-ODA@rNP + RFCA +NIR group at 10 days, S1S1 = 300 ms ≠ AA, which demonstrated that the pacing failed and that the LAA still maintained the injury state. As shown in Fig. 4G, the ratio of AA/S1S1 in the ECGs differed among all the groups. Compared with the RFCA and ICG-ODA + RFCA groups at 10 days, the ICG-ODA@rNP group had an increased AA/S1S1 ratio, which was consistent with the results obtained for the ablation area tissue sections. Furthermore, we showed the advantage of ROS-responsive double-locked liposome collaborative PDT in reducing the recovery of electrical conduction by the electrical conduction recovery ratio after RFCA in each group at 10 days (Fig. 4H). However, the treatment mechanism of ICG-ODA@rNP in vivo needs to be further investigated.

3.11. Detection of cardiomyocyte apoptosis and ROS in the ablation region

ROS serve as critical mediators of cellular signal transduction and homeostatic processes (D'Autréaux and Toledano, 2007; Shadel and Horvath, 2015; Sun et al., 2020). Under environmental changes, such as long-term ultraviolet irradiation, high glucose stimulation, or destruction of the oxidant/reducing agent balance in the body, ROS levels increase sharply, which causes oxidative damage to cellular lipids and DNA and triggers a series of pathological changes. To assess the degree of oxidative stress, cryosections of the rabbit LAA were stained with DHE, a fluorescent probe of superoxide anion. To assess the degree of oxidative stress, cryosections of the rabbit LAA was stained with DHE, a fluorescent probe of superoxide anion. After entering the cell, DHE could be oxidized by intracellular ROS to form red fluorescence. Compared to the ICG-ODA group, the post-RFCA, the ICG-ODA@rNP group showed more obvious red fluorescence, as shown in Fig. 5A-B; therefore, the ROS level in the cells of this group was significantly increased.

The TUNEL assay is a method used to detect cell apoptosis by labeling fragmented DNA ends within cells. Given that cardiomyocyte apoptosis results in DNA fragmentation, post-TUNEL staining emits green fluorescence. As shown in Fig. 5C, the control group displayed almost no green fluorescence, which implies a normal cellular status. Green fluorescence was observed in the RFCA group, albeit in limited quantities, suggesting that a subset of cardiomyocytes had experienced apoptosis. However, most cardiomyocytes appeared to have regained their vitality over time. Similarly, the ICG-ODA group showed less green fluorescence, indicating that ICG-ODA alone cannot accurately target cardiomyocytes, is quickly cleared, and cannot maximize cell death. In contrast, the ICG-ODA@rNP group exhibited pronounced bright green fluorescence, generated the highest quantity of positive cells, and caused conspicuous nuclear damage. Apoptosis was quantified, and the results were consistent with those described above (Fig. 5D). The double-locked design ensures the excellent specificity of ICG-ODA@rNP for cardiomyocytes. After NIR laser irradiation, the nanoparticles produce ROS in a chain reaction manner, which causes intracellular DNA strand breaks, promotes apoptosis, and blocks the recurrence of electrical conduction.

3.12. Bcl-2, Bax and cleaved caspase-3 quantification

High levels of ROS and oxidative stress tend to induce apoptosis. As a signaling pathway that regulates apoptosis and survival, the Bcl-2, Bax and cleaved caspase-3 signaling pathway is involved in various diseases. The Bcl-2 family plays a key role in promoting or inhibiting the endogenous apoptotic pathway caused by mitochondrial dysfunction. The ratio of Bax/Bcl-2 determines whether cells survive or undergo apoptosis. In normal organisms, cytochrome C (Cyt C) is present in the lipid bilayer of the mitochondrial inner membrane. When mitochondria are damaged, the permeability of the mitochondrial outer membrane increases, releasing Cyt C into the cytoplasm. Cleaved caspase-3 is activated to further promote the release of Cyt C, forming a positive feedback loop and triggering apoptosis. The amount of cleaved caspase-3 reflects the level of apoptosis.

The rabbits in each group were sacrificed at 10 days post-RFCA, and the levels of apoptosis markers (Bcl-2, Bax and cleaved caspase-3) in the LAA were measured by immunohistochemical analysis, as shown in Fig. 5E-H. Compared with ICG-ODA, ICG-ODA@rNP significantly downregulated the expression of Bcl-2 and increased the expression levels of Bax and cleaved caspase-3. This result indicates that ICG-ODA@rNP can effectively promote apoptosis.

3.13. Safety evaluation

As shown in Fig. 6A, no obvious pathological damage or inflammatory lesions were found in the organs (heart, liver, spleen, lung, and kidney) of each group. The results showed that ICG-ODA@rNP had no obvious systemic toxicity, and the side effects were negligible.

Cardiac markers are typical indicators for assessing myocardial injury (Ramasamy, 2011). As shown in Fig. 6B-E, the levels of CK, CK-MB, LDH and cTn-I in rabbit serum were detected. There was no
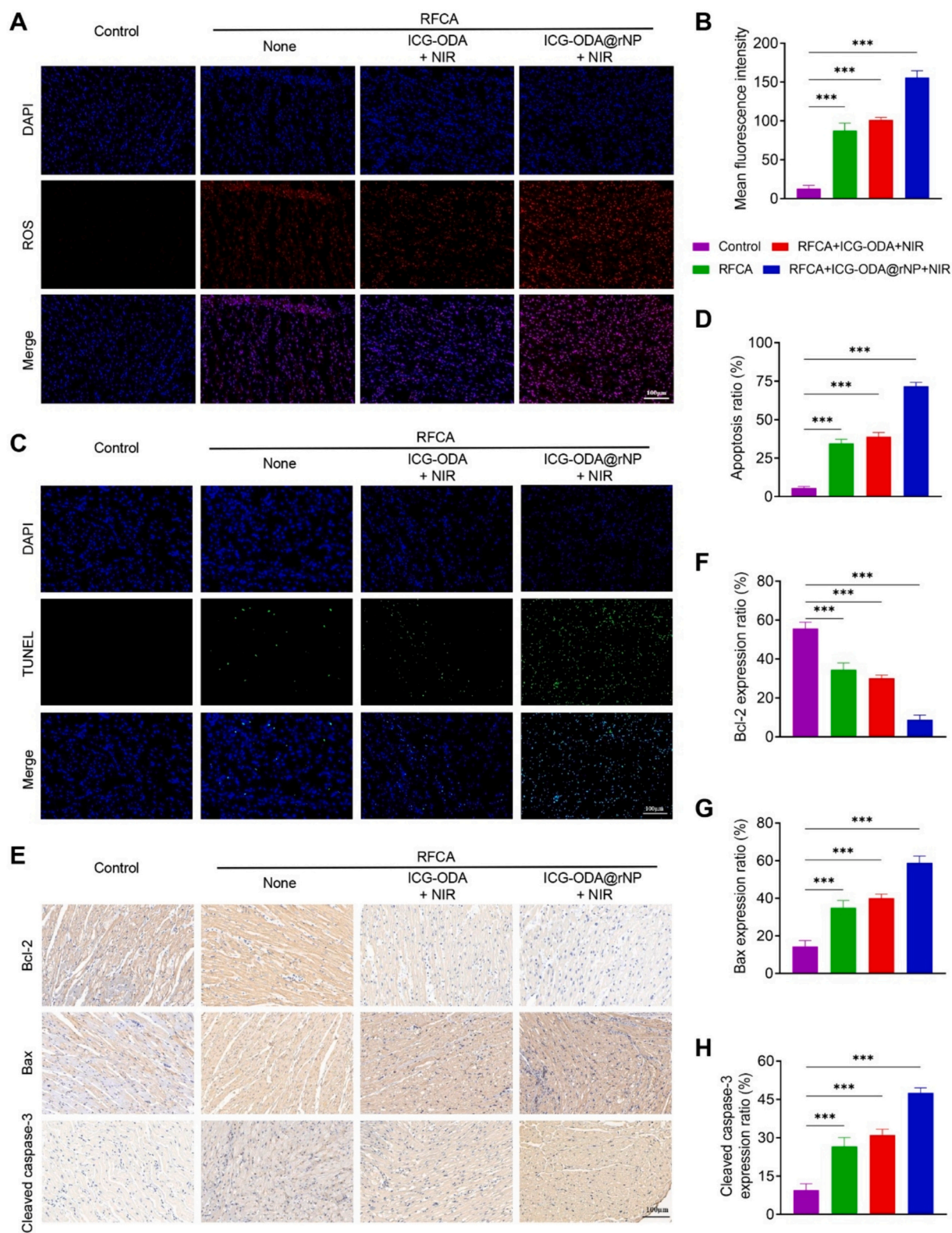
Fig. 5. Immunofluorescence analysis of the DHE probe for ROS in the left heart ear (A) and quantitative fluorescence (B). TUNEL staining was performed on the left atrial appendage of rabbits in each group (C), and the apoptosis ration of myocardial cells was quantified (D). (E) Representative Bcl-2, Bax, and cleaved caspase-3 protein levels in different treatment groups were measured *via* immunohistochemistry analysis. Bcl-2 (F), Bax (G), and cleaved caspase-3 (H) protein expression ration in each group. ***P < 0.001 compared with the control group. Data are presented as mean ± SD (n = 4).
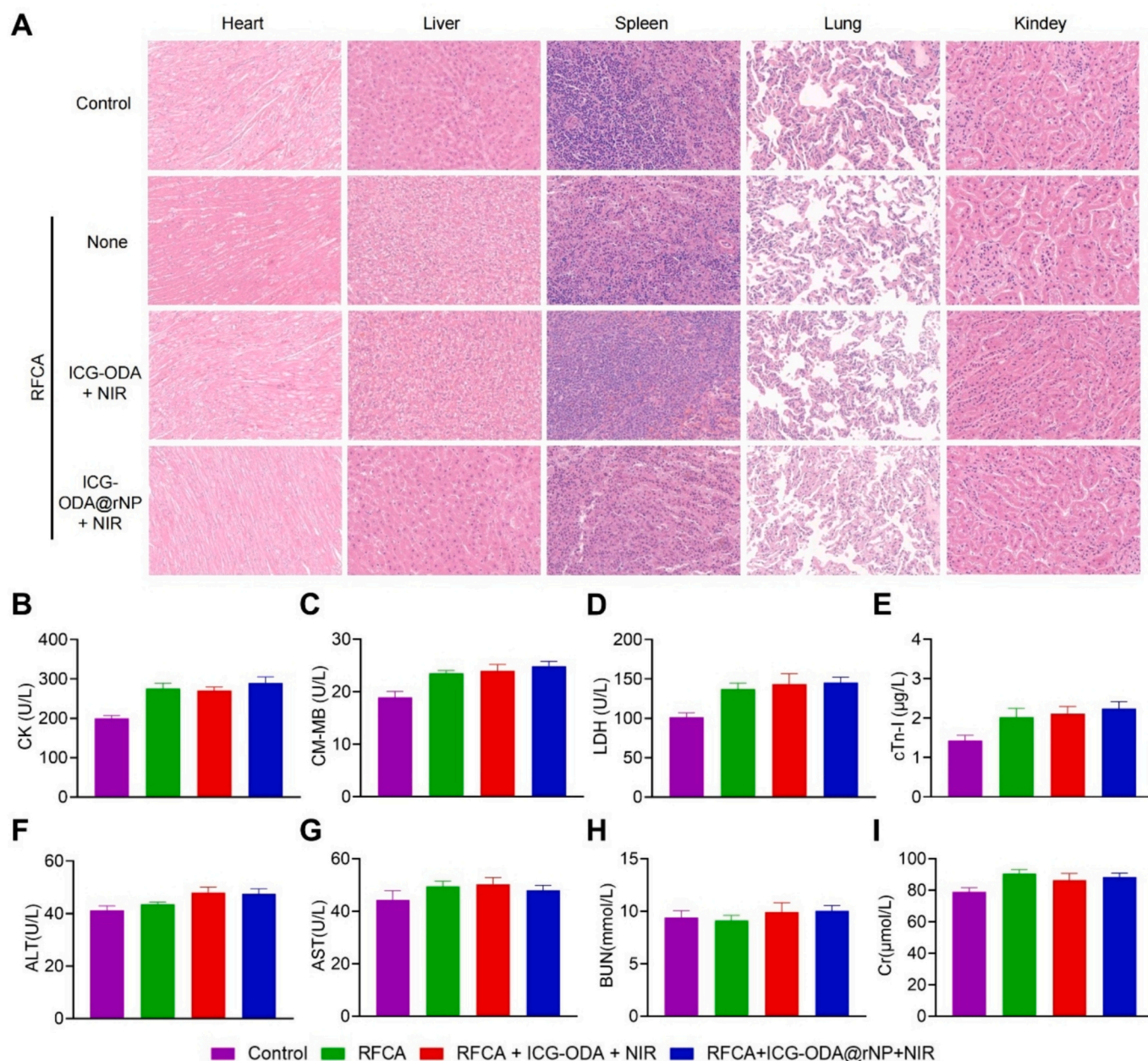
Fig. 6. Safety evaluation of ICG-ODA@rNP. (A) H&E staining of the main organs of each group on day 7 after the end of light. Levels of CK (B), CK-MB (C), LDH (D) and cTn-I (E) in each treatment group. Levels of ALT (F), AST (G), BUN (H), and Cr (I) in each treatment group. Data are presented as mean ± SD (n = 4).

significant difference between the administration group and the RFCA group at 10 days. This result indicates that despite inducing local myocardial injury, ICG-ODA@rNP does not have long-term adverse effects on overall cardiac function.

The blood of rabbits in all groups was taken for the detection of liver and kidney function. ALT and AST were used to evaluate liver function, and BUN and Cr were used to evaluate renal function. The results are shown in Fig. 6F-I. The changes in blood biochemical indices in each group were within the normal range. The results showed that the toxicity of ICG-ODA@rNP to liver and kidney function was negligible, and the *in vivo* safety of ICG-ODA@rNP was great.

4. Conclusions

In this study, new ROS-responsive 'double-locked' nanohybrid liposomes with precise targeting and release effects were developed for the treatment of electrical conduction recovery in cardiomyocytes after RFCA. First, redox-sensitive PBAP was coupled with β-CD to form OCD, and then the hydrophobically modified photosensitizer (ICG-ODA) was encapsulated to form ICG-ODA@rNP. *In vitro* drug release experiments confirmed the double-locked release characteristics of ICG-ODA@rNP. During blood circulation, ICG-ODA@rNP can selectively accumulate in the LAA. The therapeutic efficacy of ICG-ODA@rNP was validated through ECG and H&E staining, and the mechanism by which ICG-ODA@rNP inhibited the recovery of electrical conduction was explored *via* immunohistochemistry and immunofluorescence staining. This process involves the activation of ROS and the regulation of the apoptosis-related proteins Bax, Bcl-2, and cleaved caspase-3, leading to the elimination of incompletely ablated cardiomyocytes. Therefore, the developed NIR laser/ROS double-locked nanotherapeutic strategy can be used to treat the recurrence of AF. Although the study of rabbit hearts was more valuable than mice, the study in dogs or pigs could help

broaden the clinical potential of ICG-ODA@rNP (Takemiya et al., 2021). In the future, we can apply the techniques in this study to cardiac ablation injury models in dogs or pigs to better evaluate long-term efficacy and reduce interference with targeted effects caused by excessive trauma. Furthermore, the comparison and mechanism difference between ICG-ODA@rNP and our previous strategies still need to be studied (Chen et al., 2024; Ying et al., 2019).

CRediT authorship contribution statement

Ying Zhuge: Writing – original draft, Methodology, Funding acquisition, Formal analysis, Conceptualization. **Gonghao Li:** Validation, Formal analysis, Data curation. **Mingyue Sun:** Validation, Resources, Methodology, Investigation. **Jiajia Zhang:** Methodology, Investigation. **Jiafeng Zou:** Supervision. **Feng Gao:** Supervision, Project administration, Funding acquisition, Data curation. **Fang Wang:** Writing – review & editing, Visualization, Supervision, Funding acquisition.

Declaration of competing interest

The authors report no conflicts of interest.

Data availability

Data will be made available on request.

Acknowledgments

Appendix A. Supplementary data

Supplementary data to this article can be found online at https://doi.org/10.1016/j.ijpx.2024.100275.

References

Adragao, P.P., Cavaco, D., Ferreira, A.M., Costa, F.M., Parreira, L., Carmo, P., Morgado, F.B., Santos, K.R., Santos, P.G., Carvalho, M.S., Durazzo, A., Marques, H., Gonçalves, P.A., Raposo, L., Mendes, M., 2016. Safety and long-term outcomes of catheter ablation of atrial fibrillation using magnetic navigation versus manual conventional ablation: a propensity-score analysis. J. Cardiovasc. Electrophysiol. 27, S11–S16. https://doi.org/10.1111/jce.12900.
Brown, S.B., Brown, E.A., Walker, I., 2004. The present and future role of photodynamic therapy in cancer treatment. Lancet Oncol. 5, 497–508. https://doi.org/10.1016/S1470-2045(04)01529-3.
Cano, A., Alcaraz, O., Acosta, M., Arnao, M.B., 2002. On-line antioxidant activity determination: comparison of hydrophilic and lipophilic antioxidant activity using the •ASTS⁺ assay. Redox Rep. 7, 103–109. https://doi.org/10.1179/135100002125000334.
Chen, H.W., Li, F., Ge, Y.L., Liu, J.Y., Xing, X., Li, M., Ge, Z.L., Zuo, X.L., Fan, C.H., Wang, S.P., Wang, F., 2024. DNA framework-enabled 3D organization of antiarrhythmic drugs for radiofrequency catheter ablation. Adv. Mater. 13 https://doi.org/10.2147/IJN.S186267.
Cormode, D.P., Skajaa, T., van Schooneveld, M.M., Koole, R., Jarzyna, P., Lobatto, M.E., Calcagno, C., Barazza, A., Gordon, R.E., Zanzonico, P., Fisher, E.A., Fayad, Z.A., Mulder, W.J.M., 2008. Nanocrystal core high-density lipoproteins: a multimodality contrast agent platform. Nano Lett. 8, 3715–3723. https://doi.org/10.1021/nl801958b.
Correia, J.H., Rodrigues, J.A., Pimenta, S., Dong, T., Yang, Z.C., 2021. Photodynamic therapy review: principles, photosensitizers, applications, and future directions. Pharmaceutics 13, 16. https://doi.org/10.3390/pharmaceutics13091332.
Darby, A.E., 2016. Recurrent atrial fibrillation after catheter ablation: considerations for repeat ablation and strategies to optimize Success. J. Atr. Fibrillation 9, 1427. https://doi.org/10.4022/jafib.1427.
D'Autréaux, B., Toledano, M.B., 2007. ROS as signalling molecules: mechanisms that generate specificity in ROS homeostasis. Nat. Rev. Mol. Cell Biol. 8, 813–824. https://doi.org/10.1038/nrm2256.

Etrych, T., Janousková, O., Chytil, P., 2019. Fluorescence imaging as a tool in preclinical evaluation of polymer-based nano-DDS systems intended for cancer treatment. Pharmaceutics 11, 28. https://doi.org/10.3390/pharmaceutics11090471.
Feng, S.B., Hu, Y., Peng, S., Han, S.L., Tao, H., Zhang, Q.X., Xu, X.Q., Zhang, J.X., Hu, H.Y., 2016. Nanoparticles responsive to the inflammatory microenvironment for targeted treatment of arterial restenosis. Biomaterials 105, 167–184. https://doi.org/10.1016/j.biomaterials.2016.08.003.
Issac, T.T., Dokainish, H., Lakkis, N.M., 2007. Role of inflammation in initiation and perpetuation of atrial fibrillation - a systematic review of the published data. J. Am. Coll. Cardiol. 50, 2021–2028. https://doi.org/10.1016/j.jacc.2007.06.054.
Katsuki, S., Matoba, T., Koga, J., Nakano, K., Egashira, K., 2017. Anti-inflammatory nanomedicine for cardiovascular disease. Front. Cardiovasc. Med. 4, 13. https://doi.org/10.3389/fcvm.2017.00087.
Kim, Y., Nurakhayev, S., Nurkesh, A., Zharkinbekov, Z., Saparov, A., 2021. Macrophage polarization in cardiac tissue repair following myocardial infarction. Int. J. Mol. Sci. 22, 15. https://doi.org/10.3390/ijms22052715.
Kong, J., Yao, C.Y., Dong, S.Y., Wu, S.L., Xu, Y.K., Li, K., Ji, L., Shen, Q., Zhang, Q., Zhan, R., Cui, H.T., Zhou, C.P., Niu, H.G., Li, G.M., Sun, W.B., Zheng, L.M., 2021. ICAM-1 activates platelets and promotes endothelial permeability through VE-cadherin after insufficient radiofrequency ablation. Adv. Sci. 8, 14. https://doi.org/10.1002/advs.202002228.
Lellouche, N., Sacher, F., Wright, M., Nault, I., Brottier, J., Knecht, S., Matsuo, S., Lomas, O., Hocini, M., Haïssaguerre, M., Jaïs, P., 2009. Usefulness of c-reactive protein in predicting early and late recurrences after atrial fibrillation ablation. Europace 11, 662–664. https://doi.org/10.1093/europace/eup077.
Li, Q.P., Li, W., Di, H.X., Luo, L.H., Zhu, C.Q., Yang, J., Yin, X.Y., Yin, H., Gao, J.Q., Du, Y.Z., You, J., 2018a. A photosensitive liposome with NIR light triggered doxorubicin release as a combined photodynamic-chemo therapy system. J. Control. Release 277, 114–125. https://doi.org/10.1016/j.jconrel.2018.02.001.
Li, W., Li, Y.Z., Liu, Z.H., Kerdsakundee, N., Zhang, M., Zhang, F., Liu, X.Y., Bauleth-Ramos, T., Lian, W.H., Mäkilä, E., Kemell, M., Ding, Y.P., Sarmento, B., Wiwattanapatapee, R., Salonen, J., Zhang, H.B., Hirvonen, J.T., Liu, D.F., Deng, X.M., Santos, H.A., 2018b. Hierarchical structured and programmed vehicles deliver drugs locally to inflamed sites of intestine. Biomaterials 185, 322–332. https://doi.org/10.1016/j.biomaterials.2018.09.024.
Li, C.W., Hu, Y., Nie, Q., Chen, S.G., Li, G., Li, L.N., Chen, S., Tang, B., Zhang, J.X.X., 2020. A reactive oxygen species-responsive antioxidant nanotherapy for the treatment of drug-induced tissue and organ injury. Biomater. Sci. 8, 16. https://doi.org/10.1039/d0bm01660h.
Lim, H.E., Choi, C.U., Na, J.O., Choi, J.I., Kim, S.H., Kim, J.W., Kim, E.J., Han, S.W., Park, S.W., Rha, S.W., Park, C.G., Seo, H.S., Oh, D.J., Hwang, C., Kim, Y.H., 2013. Effects of iatrogenic myocardial injury on coronary microvascular function in patients undergoing radiofrequency catheter ablation of atrial fibrillation. Circ.-Arrhythmia Electrophysiol. 6, 318–326. https://doi.org/10.1161/CIRCEP.113.000282.
Lim, H.S., Schultz, C., Dang, J., Alasady, M., Lau, D.H., Brooks, A.G., Wong, C.X., Roberts-Thomson, K.C., Young, G.D., Worthley, M.I., Sanders, P., Willoughby, S.R., 2014. Time course of inflammation, myocardial injury, and prothrombotic response after radiofrequency catheter ablation for atrial fibrillation. Circ.-Arrhythmia Electrophysiol. 7, 83–89. https://doi.org/10.1161/CIRCEP.113.000876.
Liu, Y., Xu, L.L., Zhang, Q.Y., Kang, Y., Liu, L.F., Liu, Z., Wang, Y.X., Jiang, X.J., Shan, Y.Z., Luo, R.Z., Cui, X., Yang, Y., Yang, X.C., Liu, X.Q., Li, Z., 2022. Localized myocardial anti-Inflammatory effects of temperature-sensitive budesonide nanoparticles during radiofrequency catheter ablation. Research 2022, 11. https://doi.org/10.34133/2022/9816234.
Magnani, N.D., Marchini, T., Calabró, V., Alvarez, S., Evelson, P., 2020. Role of mitochondria in the redox signaling network and its outcomes in high impact inflammatory syndromes. Front. Endocrinol. 11, 15. https://doi.org/10.3389/fendo.2020.568305.
Moghimi, S.M., Hunter, A.C., Murray, J.C., 2005. Nanomedicine: current status and future prospects. FASEB J. 19, 311–330. https://doi.org/10.1096/fj.04-2747rev.
Munteanu, I.G., Apetrei, C., 2021. Analytical methods used in determining antioxidant activity: a review. Int. J. Mol. Sci. 22, 30. https://doi.org/10.3390/ijms22073380.
Odutayo, A., Wong, C.X., Hsiao, A.J., Hopewell, S., Altman, D.G., Emdin, C.A., 2016. Atrial fibrillation and risks of cardiovascular disease, renal disease, and death: systematic review and meta-analysis. BMJ-Brit. Med. J. 354, 11. https://doi.org/10.1136/bmj.i4482.
Ramasamy, I., 2011. Biochemical markers in acute coronary syndrome. Clin. Chim. Acta 412, 1279–1296. https://doi.org/10.1016/j.cca.2011.04.003.
Re, R., Pellegrini, N., Proteggente, A., Pannala, A., Yang, M., Rice-Evans, C., 1999. Antioxidant activity applying an improved ABTS radical cation decolorization assay. Free Radic. Biol. Med. 26, 1231–1237. https://doi.org/10.1016/s0891-5849(98)00315-3.
Shadel, G.S., Horvath, T.L., 2015. Mitochondrial ROS signaling in organismal homeostasis. Cell 163, 560–569. https://doi.org/10.1016/j.cell.2015.10.001.
Sprague, A.H., Khalil, R.A., 2009. Inflammatory cytokines in vascular dysfunction and vascular disease. Biochem. Pharmacol. 78, 539–552. https://doi.org/10.1016/j.bcp.2009.04.029.
Sun, Y., Lu, Y.F., Saredy, J., Wang, X.W., Drummer, C., Shao, Y., Saaoud, F., Xu, K.M., Liu, M., Yang, W.Y., Jiang, X.H., Wang, H., Yang, X.F., 2020. ROS systems are a new integrated network for sensing homeostasis and alarming stresses in organelle metabolic processes. Redox Biol. 37, 21. https://doi.org/10.1016/j.redox.2020.101696.
Sun, L.N., Fan, M.R., Huang, D., Li, B.Q., Xu, R.T., Gao, F., Chen, Y.Z., 2021. Clodronate-loaded liposomal and fibroblast-derived exosomal hybrid system for enhanced drug

delivery to pulmonary fibrosis. Biomaterials 271, 14. https://doi.org/10.1016/j. biomaterials.2021.120761.

Takemiya, K., Roise, J.J., He, M.M., Taing, C., Rodriguez, A.G., Murthy, N., Goodman, M. M., Taylor, W.R., 2021. Maltohexaose-indocyanine green (MH-ICG) for near infrared imaging of endocarditis. PloS One 16, 12. https://doi.org/10.1371/journal. pone.0247673.

Yan, X.X., Anzai, A., Katsumata, Y., Matsuhashi, T., Ito, K., Endo, J., Yamamoto, T., Takeshima, A., Shinmura, K., Shen, W.F., Fukuda, K., Sano, M., 2013. Temporal dynamics of cardiac immune cell accumulation following acute myocardial infarction. J. Mol. Cell. Cardiol. 62, 24–35. https://doi.org/10.1016/j. yjmcc.2013.04.023.

Ying, Z.G., Zheng, Z.F., Xie, M.Q., Li, L., Wang, F., Gao, F., 2016. Preparation of liposomal amiodarone and investigation of its cardiomyocyte-targeting ability in cardiac radiofrequency ablation rat model. Int. J. Nanomedicine 11, 2359–2367. https://doi.org/10.2147/IJN.S98815.

Ying, Z.G., Ni, H.E., Wang, Y.J., He, M.Y., Wang, J.S., Gao, F., Wang, F., 2019. Combination of doxorubicin liposomes with left atrial appendage radiofrequency catheter ablation to reduce post-ablation recovery of electrical conduction. Int. J. Nanomedicine 14, 231–241. https://doi.org/10.2147/IJN.S186267.

Yuan, Z.T., Liu, C.L., Sun, Y.J., Li, Y., Wu, H.L., Ma, S.L., Shang, J., Zhan, Y.P., Yin, P.H., Gao, F., 2022. Bufalin exacerbates photodynamic therapy of colorectal cancer by targeting SRC-3/HIF-1α pathway. Int. J. Pharm. 624, 12. https://doi.org/10.1016/j. ijpharm.2022.122018.

Zhang, Q.X., Zhang, F.Z., Chen, Y., Dou, Y., Tao, H., Zhang, D.L., Wang, R.B., Li, X.H., Zhang, J.X., 2017. Structure-property correlations of reactive oxygen species-responsive and hydrogen peroxide-eliminating materials with anti-oxidant and anti-inflammatory activities. Chem. Mat. 29, 8221–8238. https://doi.org/10.1021/acs. chemmater.7b02412.

Zhang, Q.X., Zhang, F.Z., Li, S.S., Liu, R.F., Jin, T.T., Dou, Y., Zhou, Z.H., Zhang, J.X., 2019. A multifunctional nanotherapy for targeted treatment of colon cancer by simultaneously regulating tumor microenvironment. Theranostics 9, 3732–3753. https://doi.org/10.7150/thno.34377.

Zou, J.F., Sun, R., He, M.Y., Chen, Y., Cheng, Y., Xia, C.H., Ma, Y., Zheng, S.L., Fu, X.Z., Yuan, Z.T., Lan, M.B., Lou, K.Y., Chen, X.J., Gao, F., 2023. Sequential rocket-mode bioactivating ticagrelor prodrug nanoplatform combining light-switchable diphtherin transgene system for breast cancer metastasis inhibition. ACS Appl. Mater. Interfaces 15, 53198–53216. https://doi.org/10.1021/acsami.3c11594.